UNIVERSITÀ DEGLI STUDI DI TRIESTE

Numerical investigation of liquid and supercritical CO2 flow behaviors through 3D self-affine rough fractures

This is the peer reviewed (post-print) version of the following article:

Original
Numerical investigation of liquid and supercritical CO2 flow behaviors through 3D self-affine rough fractures / Li, J., Li, Z.i., Yuan, W., Lei, X., Andres Galindo Torres, S., Cherubini, C., Scheuermann, A., Li, L.. - In: FUEL. - ISSN 0016-2361. - ELETTRONICO. - 251/2019:(2019), pp. 669-682. [10.1016/j.fuel.2019.04.012]

Availability:
This version is available at: 11368/3059699 since:

Publisher:

Published
DOI:10.1016/j.fuel.2019.04.012

Terms of use:

Some rights reserved. More details in the PostPrint rights section below.

License:
Attribution-NonCommercial-NoDerivatives 4.0 International

Publisher copyright

-.-

(Article begins on next page)

19 October 2026

arTs Università degli Studi di Trieste
Archivio della ricerca – postprint

Numerical investigation of liquid and supercritical CO_2 flow behaviors through 3D self-affine rough fractures

Jiawei Li[a,*], Zi Li[d], Wanju Yuan[b], Ximing Lei[a], Sergio Andres Galindo Torres[d], Claudia Cherubini[c], Alexander Scheuermann[a], Ling Li[d]

[a] School of Civil Engineering, University of Queensland, Brisbane 4072, Australia
[b] Faculty of Engineering and Applied Science, University of Regina, Regina S4S 0A2, Canada
[c] Department of Physics and Earth Sciences, University of Ferrara, via Saragat 1, 44122 Ferrara, Italy
[d] School of Engineering, Westlake University, Hangzhou 310024, China

ARTICLE INFO

Keywords:
CO_2 properties
Rough fracture surfaces
Tortuosity
Streamlines

ABSTRACT

In recent years, CO_2 has been utilized to be injected into natural and induced fracture reservoirs with the purpose of enhanced natural energy resources recovery. In this study, the influence of liquid and supercritical CO_2 properties under different pressure and temperature conditions on flow behaviors through a 3D self-affine fracture with rough surfaces is investigated with the application of Lattice Boltzmann method (LBM). CO_2 has properties highly dependent on pressure and temperature and this study focuses on the liquid and supercritical CO_2 properties because it is very common for CO_2 to maintain liquid and supercritical states in deep reservoirs. LBM was used to simulate liquid and supercritical CO_2 flow through a single fracture with rough surfaces. In addition to CO_2 properties, the effects of pressure differences between the injecting and discharging surfaces of the fracture were also considered. The density and dynamic viscosity of CO_2 display similar trends in responses to changes in pressure and temperature. Simulation results show that the average velocity of CO_2 flow changes considerably with temperatures and pressures. The streamlines distributions revealed the changes of tortuosity under different temperature and pressure conditions, which follows a similar trend to that of the average velocity. A detailed analysis of the effects of the temperature, pressure and upscaling velocity on tortuosity was conducted based on the relevant curves and streamlines distributions. It was found that the values of tortuosity have a close relationship with the kinematic viscosity, which depends on temperature and pressure conditions.

1. Introduction

The technologies for carbon capture, utilization and storage (CCUS) have been developed and implemented to reduce CO_2 emissions in the last decades [1–3]. There are several CO_2 utilization methods that have been applied in energy areas with taking CO_2 storage in the reservoirs into consideration, including CO_2 flooding, liquid CO_2 fracturing, enhanced geothermal systems (EGS) and methane displacement from gas hydrates [4–10]. In addition, the supercritical temperature and pressure for CO_2 is 31.04 °C and 7.38 MPa, which means it is easy for CO_2 to keep its liquid and supercritical states under reservoir conditions (oil, gas and geothermal) [11–13]. Therefore, the understanding of liquid and supercritical CO_2 through a fracture has a great significance for modelling CO_2 flow efficiently and accurately in natural and induced fractured reservoirs.

In recent years, many studies have mainly focused on investigating the fracture propagation process and flow in the fracture networks of liquid and supercritical CO_2 as fracturing liquids through field testing, laboratory experiments and simulations [14–19]. The leak off properties of liquid CO_2 fracturing are presented based on field and laboratory measurements [20]. The growth behaviours of fractures induced by supercritical CO_2 in tight sandstones were explored through a series of experiments under triaxial stress conditions [21]. The effects of water and supercritical CO_2 on fracture propagation behaviours were compared, indicating that supercritical CO_2 creates shorter fractures in comparison with water under similar injection conditions [22]. And CO_2 has been used to improve geophysical identification and characterization of fractures and faults in push-pull well tests at enhanced geothermal system sites [23]. In addition, with taking CO_2 properties into consideration, a phase state control model was developed to simulate supercritical CO_2 fracturing under different temperatures [24].

As for mathematical model of the fluid flow through a fracture, the

* Corresponding author.
E-mail address: jiawei.li001@gmail.com (J. Li).

Nomenclature

C	the characteristic lattice velocity in a cell size
e_i	velocity in the i-th direction in a LBM cell
D_f	fractal dimension
H	Hurst exponent
L	Characteristic length
r	a constant value
t	time
P	pressure
T	temperature
V	velocity magnitude
u	velocity in LBM
X, Y, Z	directions

Greek symbols

ρ	density
σ	standards deviation
τ	the relaxation time
μ	the dynamic viscosity
υ	the kinematic viscosity
Ω_{col}	the collision operator
ω_i	the weight factor in the i-th direction
δ_x	the length of each grid
δ_t	the length of time step

Parallel Plate theory for the characterization of fractures has been the most popular method due to its convenience for quantitative analysis [25–28]. However, the complex roughness of natural fracture surfaces under reservoir conditions is ignored. In order to gain a better characterization of fluid flow into a fracture, it is of critical importance to investigate the effects of rough surfaces of the fracture. Though the fracture roughness is very complex, some experimental methods, such as X-ray computed tomography, have been proposed to characterize fracture roughness efficiently [29–31]. Different experiments of water flow through a single fracture have been designed to examine the effects of fracture surface roughness, apertures and Reynolds number [32–38]. The experimental investigations of water flow paths through natural rough fractures with the application of tracer have been presented [39]. Combined with the experiments under confining pressure, the aperture distributions and fluid flow through a single rough facture are characterized [40]. In addition to the experiments, mathematical methods and theories have been developed to the modelling of fluid flow through a fracture more accurately. A more accurate solution corresponding to the Navier-Stokes equations was introduced to describe fluid flow between slightly rough surfaces of real fractures [41]. The classical Local Cubic Law with considering the fact that various values of fracture apertures are distributed in spatial locations was proposed [42]. The use of various simplifications and applied ranges of Reynolds Lubrication equation for fluid flow into a fracture were discussed and evaluated [43,44]. A model that corporates surface geometry of natural fractures has been upgraded with the purpose of channelling flow evaluation [45]. And a modified Local Cubic Law that a low range of local Reynolds Numbers can be applied was developed, which also integrates fracture surface roughness and local tortuosity [46].

The Lattice Boltzmann method has been applied for mathematical model and simulation of fluid flow through a fracture with rough surfaces in the 21st century [47,48]. It is shown that fracture anisotropy has a greater effect on the fracture permeability compared with the mean aperture and fractal dimension of the fracture by analysing the flow behaviours through a fracture with rough surfaces on the basis of Lattice Boltzmann simulations [49]. The LBM was also used to investigate the influence of wettability for different fluids on corresponding interfacial areas in a rough fracture with self-affinity [50]. In addition, influences of main and secondary roughness for fracture surfaces on nonlinear behaviours of water flow in 3D rough fractures with the characteristic of self-affinity were analysed with the application of the LBM [51]. Another study shows that with the increase of fracture roughness, the eddy volumes become larger and the effective hydraulic conductivities decreases in rough fractures [52]. An experiment has been designed for the investigation of water flow through fractures with rough surfaces that are generated by 3D printing technology and then the experimental results are compared with simulation results from LBM [53].

In recent years, investigations of liquid and supercritical CO_2 through a single rough fracture are very limited, but several studies on heat transfer of water flow through rough fractures [54–57]. The influences of supercritical CO_2 flow on the heat transfer and spatial distributions on the rough fracture surface was studied with the finite volume method [19]. In this paper, the effects of relevant factors, including liquid and supercritical CO_2 properties, fracture surface roughness etc, on flow behaviors are presented and analysed when liquid and supercritical CO_2 flow into a rough fracture.

2. Self-affine rough fracture surfaces

In order to reflect the rough surfaces of natural fractures accurately,

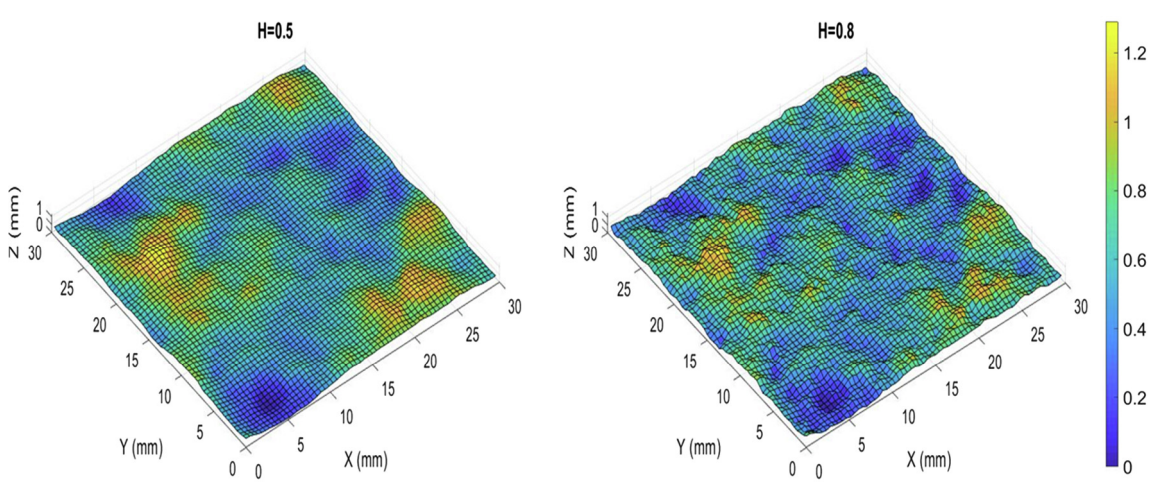

Fig. 1. Two self-affine fracture bottom surfaces corresponding to different Hurst exponents with σ = 0.2 mm.

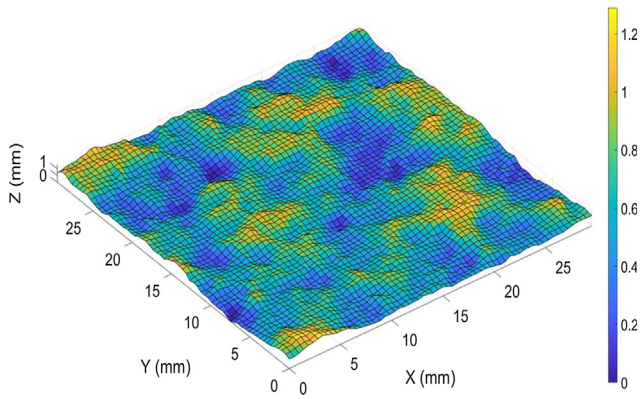

Fig. 2. A self-affine fracture aperture distributions with $\sigma = 0.2$ mm and $H = 0.6$.

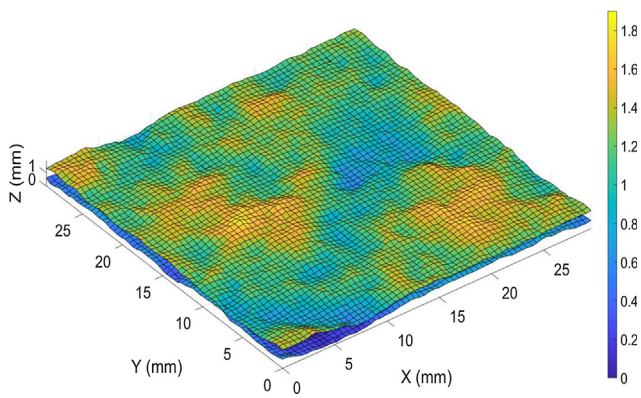

Fig. 3. The top and bottom surfaces of the fracture with $\sigma = 0.2$ mm and $H = 0.6$.

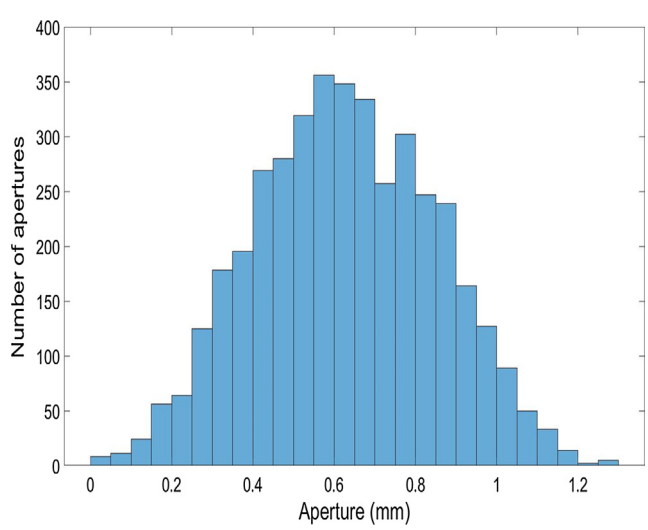

Fig. 4. Statistical histogram of the apertures in a self-affine rough fracture with $\sigma = 0.2$ mm and $H = 0.6$.

the fractal theory has been applied to create the rough fracture surfaces with the characteristic of self-affinity artificially [58–60]. The self-affinity is a characteristic of a fractal whose pieces can be scaled by different amounts along X and Y directions, meaning that the self-similarity of these fractal objects can be observed [61,62]. And an anisotropic affine transformation should be used to rescale and test the self-affinity [61].

The variance of the surface height is defined as follows [63]:

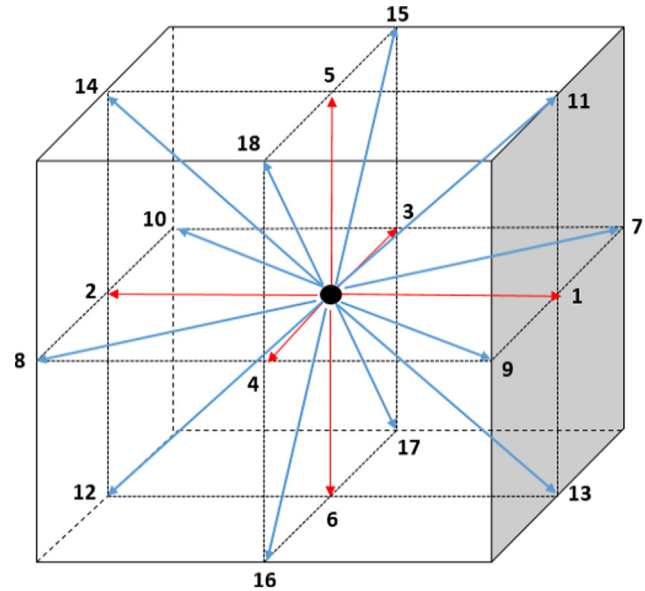

Fig. 5. D3Q19 model: velocity vectors in a cell.

$$\sigma^2(r) = \langle [Z(x + rh_x, y + rh_y) - Z(x, y)]^2 \rangle \tag{1}$$

where σ^2represents the variance, $r$is a constant and $Z$is the surface height, h is the increment of surface height along X and Y directions.

When Hurst exponent is used for fracture generation, its range is usually between 0 and 1. It should be noticed that the values of Hurst exponent have been found to locate in the range of 0.45 and 0.85 in most cases [59,64]. In addition, it has been mentioned that the fracture roughness follows a self-affine distribution that is produced by the fractal dimension. Here the fractal dimension D_f has the following relationship with the Hurst exponent [59]:

$$D_f = 3 - H \tag{2}$$

Another important parameter, power spectral density ratio, is also used for the generation of rough fracture surfaces, which considers the variation between the top and bottom fracture surfaces [65,66].

On the basis of the proposed theories, the self-affine fracture with rough surfaces have been generated by using the 64 × 64 data sets from the software SynFrac [66]. And Matlab R2017a has been used to deal with the data sets from SynFrac. The examples of self-affine fracture surfaces corresponding to different values of Hurst exponents with remaining other variables that affect fracture rough surfaces constant are shown in Fig. 1. The length and width of fracture models are both 30 mm and there are grids distribution on the X-Y plane in order to reflect 64 × 64 data sets of heights that varies due to self-affine fracture roughness. As is shown in Fig. 1 the heights follows a self-affine fractal distribution and the heights of several grids increase with Hurst exponent increasing.

In this study, a schematic of apertures that is with $\sigma = 0.2$ mm for the generated fracture surfaces with $H = 0.6$ shown in Fig. 2 will be used for further simulations. In Fig. 2, deeper blue colors reflect the smaller apertures, up to zero, and larger values of apertures are represented by brighter yellow colors, which will be combined with streamlines distributions for analysis. The corresponding top and bottom surfaces are shown in Fig. 3. The statistical histogram of apertures of a self-affine fracture with $\sigma = 0.2$ mm and $H = 0.6$ is shown in Fig. 4.

3. Lattice Boltzmann method (LBM)

The LBM is a highly efficient method that simulates single and multiphase flow systems under the conditions of complex geometries,

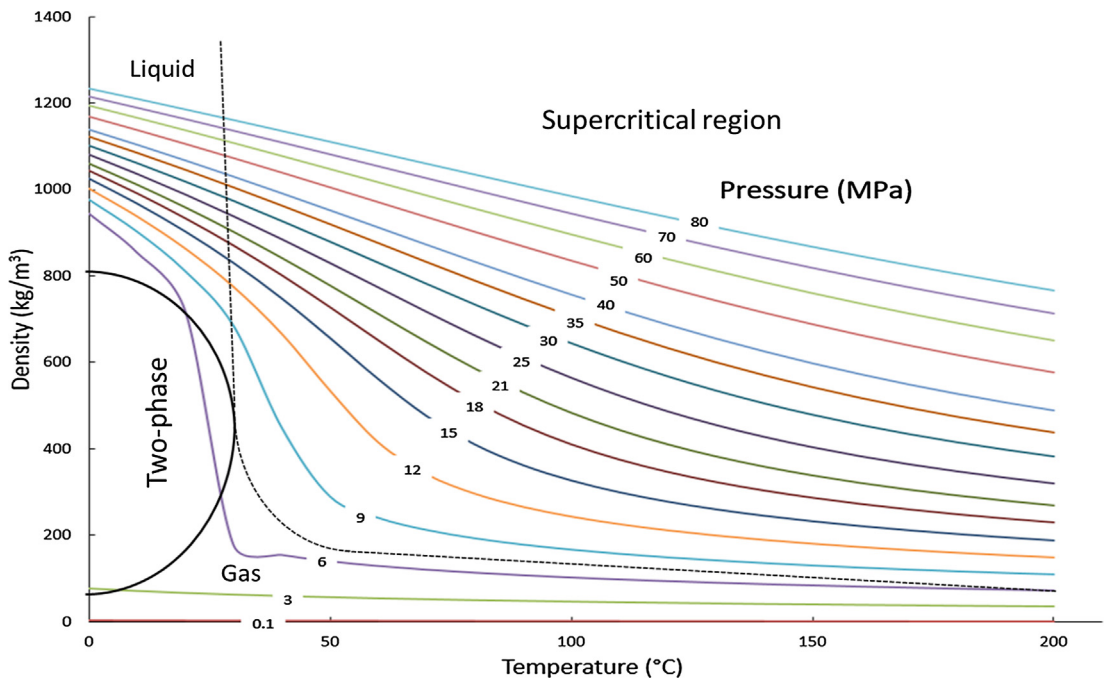

Fig. 6. CO_2 density corresponding to temperature and pressure.

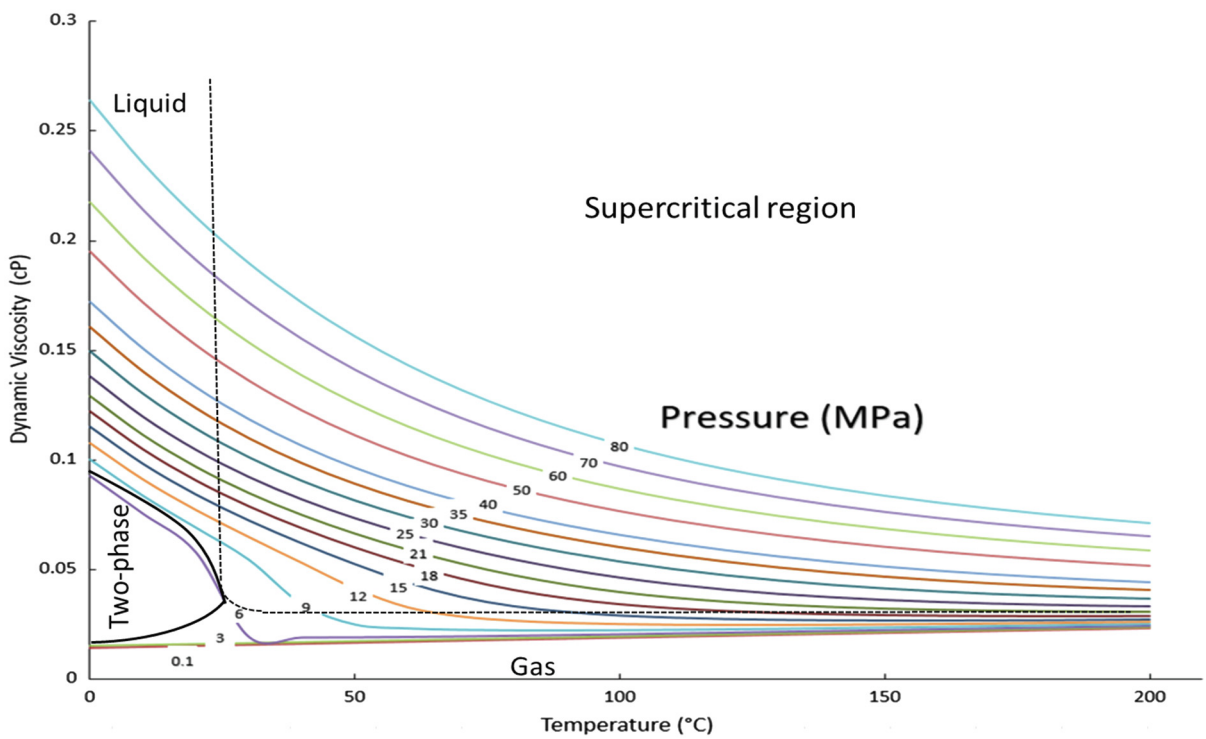

Fig. 7. CO_2 dynamic viscosity corresponding to temperature and pressure.

which has been applied in different areas, such as fluids flow though porous media and fractures, thermal fluids flow etc. [67–71]. In this paper, a D3Q19 model was used to simulate liquid and supercritical CO_2 through a single fracture model [72]. There are nineteen discrete velocities distributed in a cubic space shown in Fig. 5.

$$\vec{e_i} = \begin{cases} 0, & i = 0, \\ (\pm 1, 0, 0), (0, \pm 1, 0), (0, 0, \pm 1), & i = 1 - 6, \\ (\pm 1, \pm 1, 0), (\pm 1, 0, \pm 1), (0, \pm 1, \pm 1) & i = 7 - 18. \end{cases} \tag{3}$$

The distribution function satisfying the evolution rule based on the Chapman-Enskog expansion of the Boltzmann equation is shown as follows [73]:

$$f_i(\vec{x} + \vec{e_i}\delta_t, t + \delta_t) = f_i(\vec{x}, t) + \Omega_{col} \tag{4}$$

where $f_i(\vec{x}, t)$ is the fluid particle distribution function with velocity $\vec{e_i}$ (the mesoscopic velocity in the i-th direction) at position $\vec{x}$ and time t, δ_t is the length of time step and $\Omega_{col}$is the collision operator representing the relaxation process due to the collision of the fluid particles.

The Bhatnagar-Gross-Krook model for the collision operator is applied here [68]:

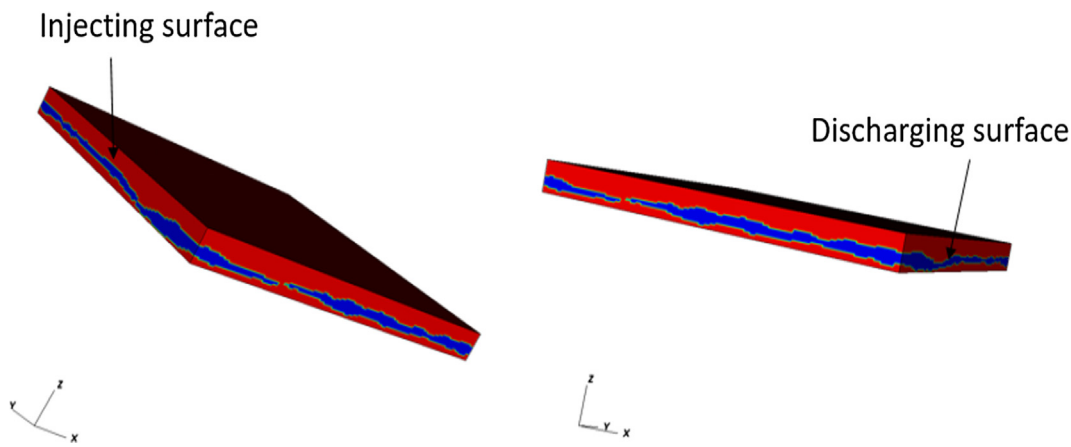

Fig. 8. Schematic of the self-affine rough fracture model from injecting and discharging surfaces.

$$\Omega_{col} = \frac{\delta_t}{\tau}(f_i^{eq} - f_i) \tag{5}$$

where τ is the relaxation time and f_i^{eq} is the equilibrium distribution.

And the relaxation time τ is the parameter that governs the rate at which the fluid tends towards equilibrium with the following expression [67]:

$$\tau = \frac{3\upsilon\delta_t}{\delta_x^2} + 0.5 \tag{6}$$

where υ is the kinematic viscosity of fluid.

The f_i^{eq} is expressed as follows:

$$f_i^{eq} = \omega_i\rho\left(1 + 3\frac{\vec{e_i}\cdot\vec{u}}{C^2} + \frac{9(\vec{e_i}\cdot\vec{u})^2}{C^4} - \frac{3u^2}{2C^2}\right) \tag{7}$$

with $C = \delta_x/\delta_t$ defined as a characteristic lattice velocity in a cell size. The density $\rho$and the velocity $\vec{u}$ at a cell position $\vec{x}$ can be calculated respectively as:

$$\rho(\vec{x}) = \sum_{i=0}^{18} f_i(\vec{x}) \tag{8}$$

$$\vec{u}(\vec{x}) = \frac{\sum_{i=0}^{18} f_i(\vec{x})\vec{e_i}}{\rho(\vec{x})} \tag{9}$$

Similar to the D3Q15 model, the weight factors in the D3Q19 model are:

$$\omega_i = \begin{cases} 1/3, & i = 0, \\ 1/18, & i = 1 - 6, \\ 1/36, & i = 7 - 18. \end{cases} \tag{10}$$

The relationship between pressure and density in LBM is defined as [67]:

$$P = \frac{1}{3}C^2\rho \tag{11}$$

4. Numerical modelling

To evaluate the influence of liquid and supercritical CO_2 properties on flow behaviors through a self-affine rough fracture, Equation of State is an efficient method to calculate relevant properties, such as density and viscosity, under different temperatures and pressures. The calculations of liquid and supercritical CO_2 properties have been realized by a commercial software (WinProp, CMG) on the basis of Peng-Robinson Equation of State. It should be noticed that the supercritical temperature and pressure for CO_2 is 31.04 °C and 7.38 MPa. Figs. 6 and 7 show the changes in density and dynamic viscosity of CO_2 with different pressures and temperatures. It can be seen that there are four regions in both Figs. 6 and 7: gas, liquid, two-phase and supercritical regions. The chosen temperature and pressure ranges should satisfy the existence of liquid and supercritical CO_2. In this study, the temperature range corresponding to CO_2 is between 20 and 100 °C and the pressure is from 10 to 60 MPa. With the gravity effect being also neglected. In addition, flow behaviours of CO_2 under certain temperature and pressure has been investigated with a series of pressure gradients between the injecting and discharging surfaces.

In order to gain a more realistic simulation of liquid and supercritical CO_2 flow through self-affine rough fractures, the numerical fracture model should reflect the fracture geometries accurately. The fracture model shown in Fig. 3 will be used for further numerical simulations. Its length and width equal to 30 mm and its height is no more than 2 mm with the solid boundary sealed on top and bottom surfaces. The fracture parameters including $\sigma = 0.2$ mm, $H = 0.6$ are kept constant. Because the fracture model is built based on the 64 × 64 data sets, the 30 mm × 30 mm X-Y plane can be divided into 256 × 256 grids. This means a resolution of 0.1171875 mm in X, Y and Z directions are used for the fracture model, which takes both fracture surface characterization and computational efficiency into consideration.

Fig. 8 shows the injecting and discharging surfaces of the fracture model in the Lattice Boltzmann domain. As is shown in Fig. 8, the red color represents the solid rock and the blue color illustrates fracture space between the top and bottom fracture surfaces. The lateral sides of fracture model are set as periodic boundaries and the fracture model is assumed to be non-deformable during the flowing process. Here periodic boundary condition is adopted to have a better schematic of the fracture model. The simulation results calculated by the periodic and solid boundary condition are compared for the validation of calculating accuracy. When the pressure difference between the injecting and discharging surfaces equals to 0.01 Pa, the average velocities for the solid boundary under the pressure condition 40 MPa and temperature condition 20 °C are 4.7227×10^{-6} m/s and the average velocity of the periodic boundary equals to 4.97×10^{-6} m/s at the same conditions, with a relative difference of 4.97%. The simulation results of the solid boundary are a little smaller than those of the periodic boundary because the initial velocities on the solid boundary equals to zero. In addition, a smaller resolution of 0.05859375 mm in X, Y and Z directions has been used to check the mesh independence. With the same conditions, the average velocities for a smaller resolution is 5.189×10^{-6} m/s. The comparisons show that the periodic boundary and resolution settings meet the simulation requirements for the research goal in this study.

There are four different pressure differences between the injecting and discharging surfaces: 10, 1, 0.1 and 0.01 Pa that are used for the following simulations under different pressure and temperature

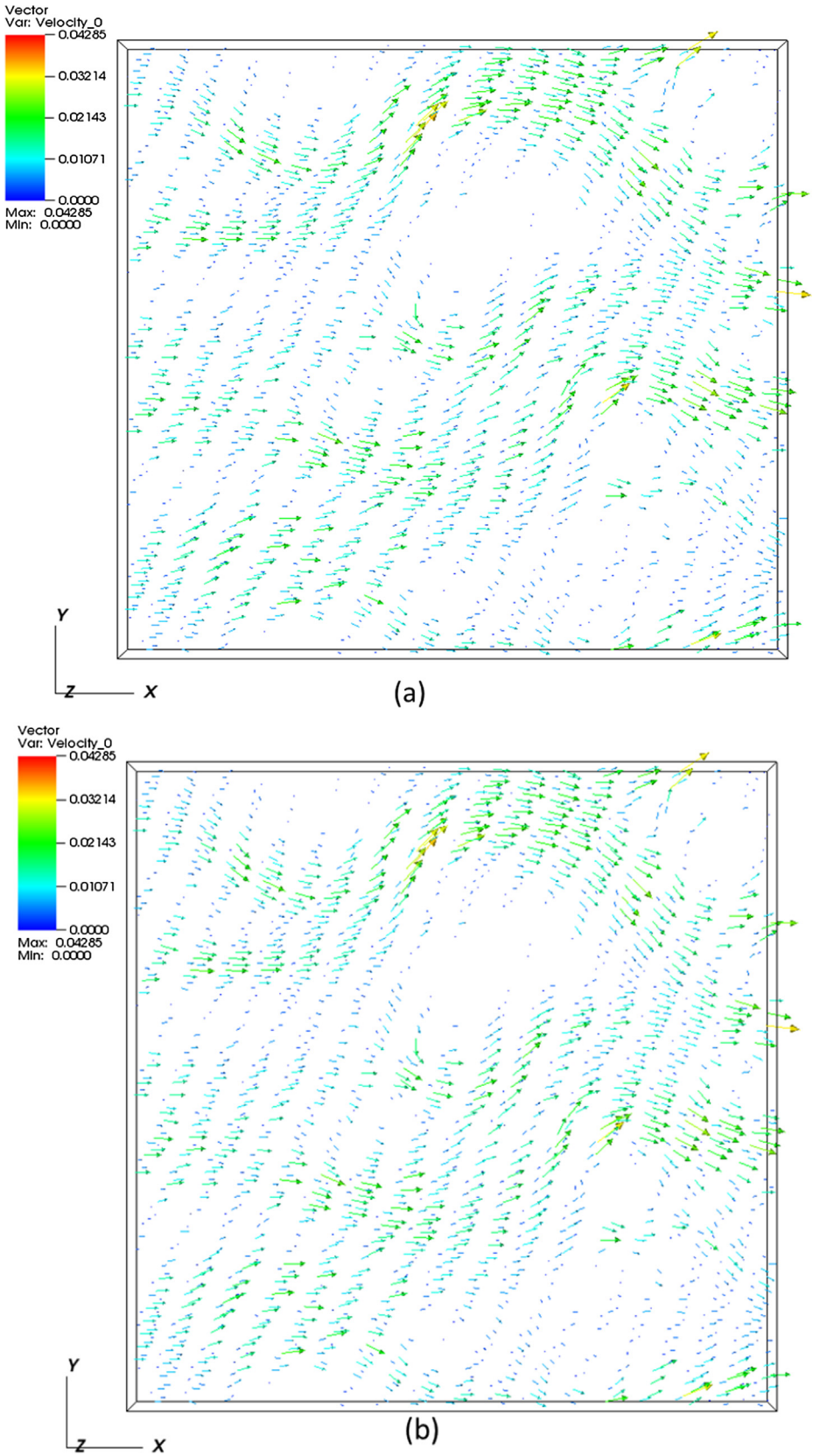

Fig. 9. Velocity vector distributions and magnitude for (a) $t_a = 40,000ts$ and (b) $t_a = 50,000ts$.

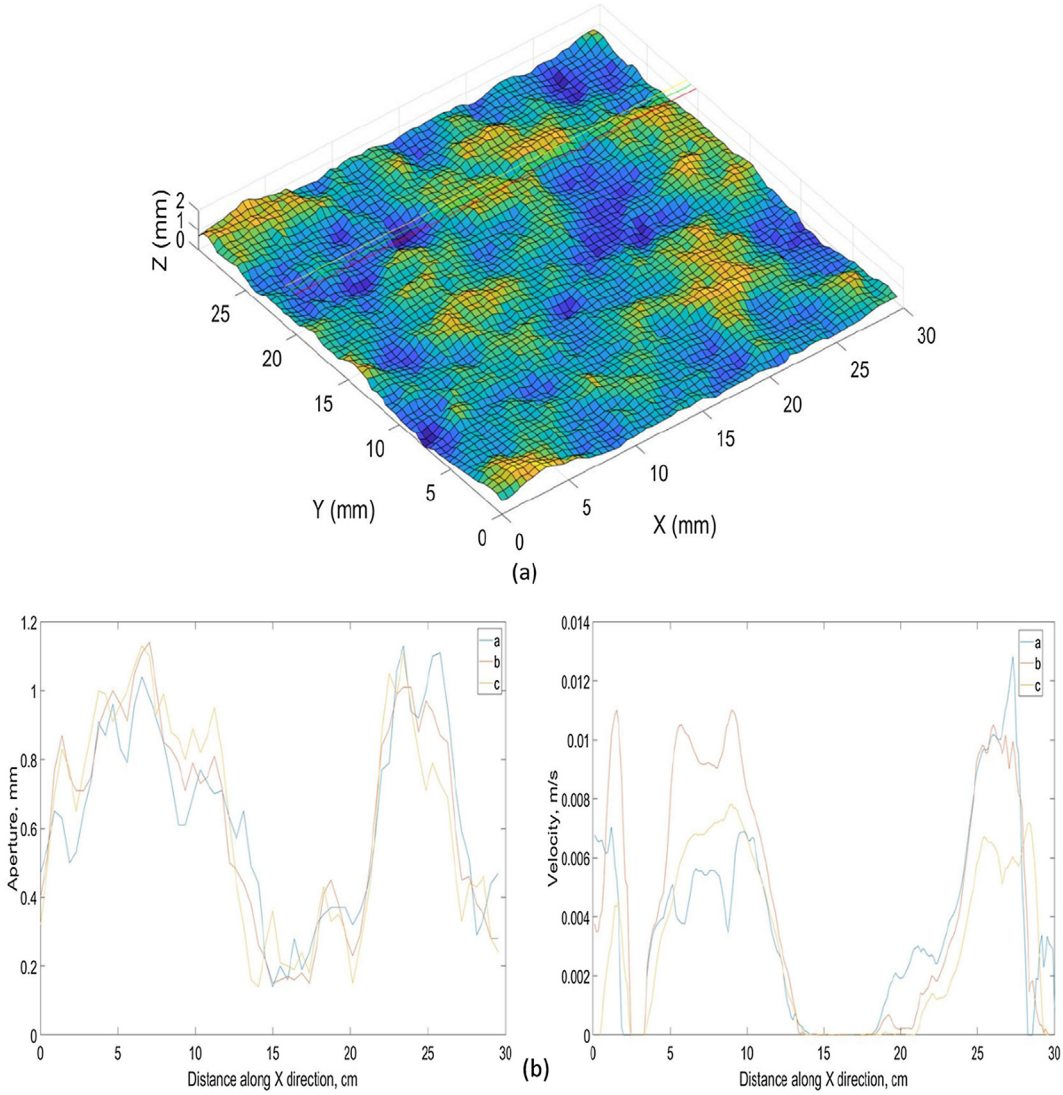

Fig. 10. (a) Schematic of three transects a, b and c and (b) corresponding aperture and velocity distributions.

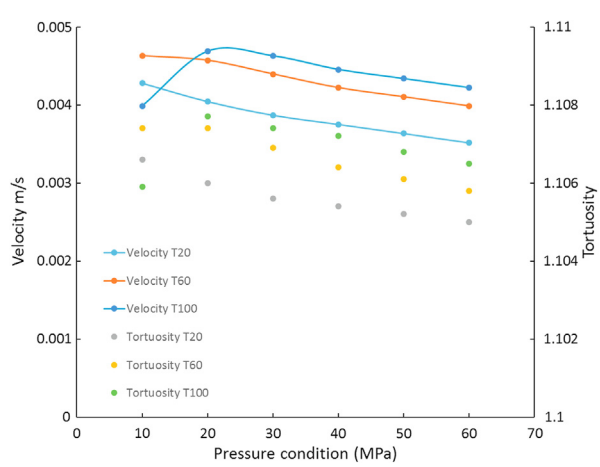

Fig. 11. Velocity and tortuosity for different pressure conditions with $\Delta p = 10$ Pa.

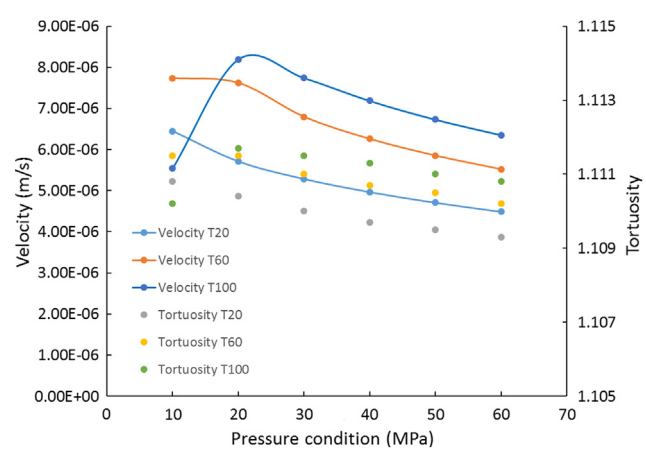

Fig. 12. Velocity and tortuosity for different pressure conditions with $\Delta p = 0.01$ Pa.

conditions in this study. The changes of CO_2 density caused by such mall pressure differences can be negligible directly, which means CO_2 densities under different pressure and temperature conditions can be assumed to be constant. In addition, it should be noticed that there are no phase transitions between liquid and supercritical CO_2 due to the same reasons. The heat transfer and spatial variations are also neglected with the temperature assumed to be constant because small scale of the fracture model and the pressure differences between the injecting and discharging surfaces are pretty small. As for transformation between

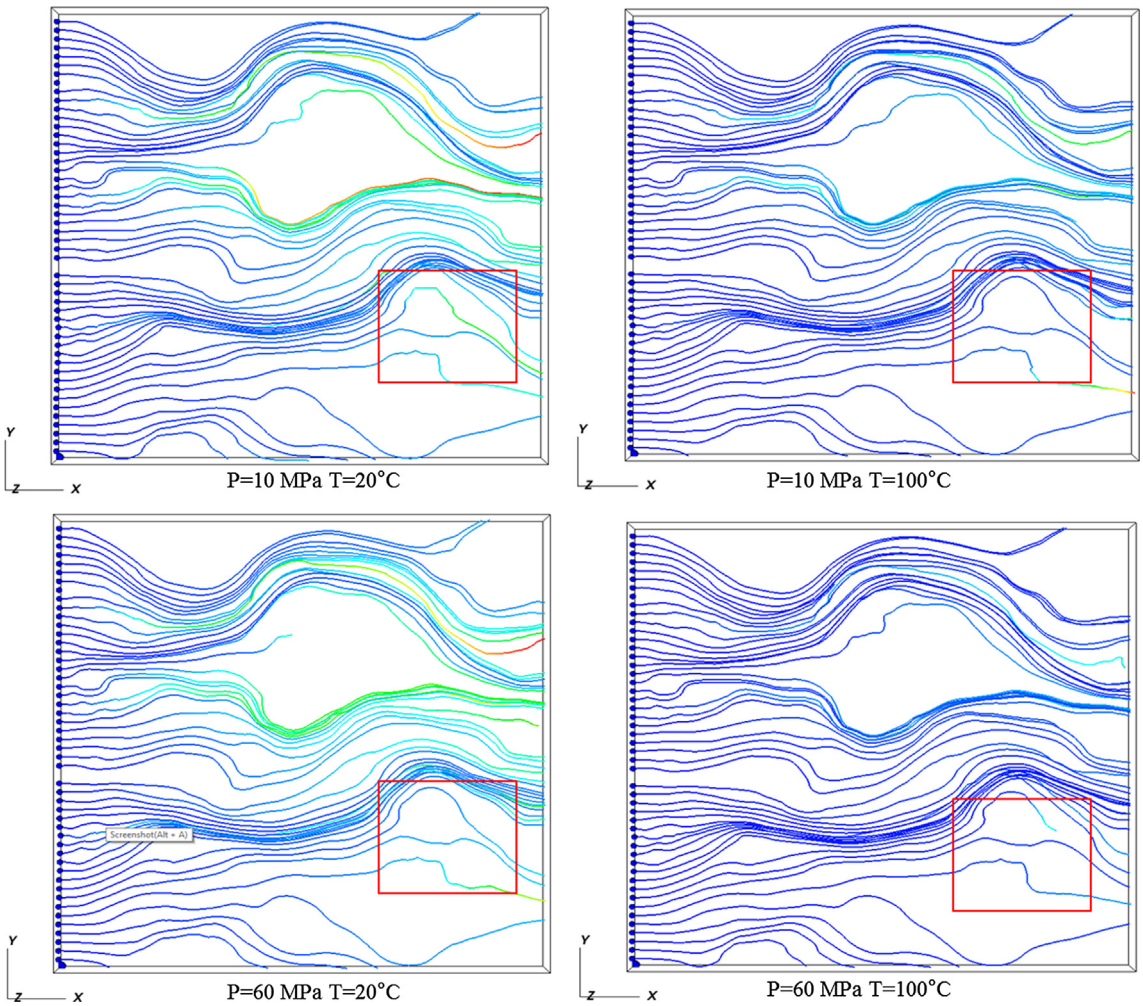

Fig. 13. Streamlines for P = 10 and 60 MPa with T = 20 and 100 °C with Δp = 10 Pa.

Table 1
Comparisons of tortuosity differences between the surrounded and whole areas at different pressure conditions.

	Tortuosity of P = 10 MPa	Tortuosity of P = 60 MPa	Tortuosity differences in the surrounded area	Tortuosity differences of the whole area
T = 20 °C	1.1754	1.1785	0.0031	0.0016
T = 100 °C	1.1742	1.1755	0.0013	0.0006

real physical and lattice Boltzmann units, the following equations can be used with considering the fact that there are single liquid or supercritical CO_2 flow in the simulations [74]:

$$\mathrm{Re} = \frac{u_{real} L_{real}}{\upsilon_{real}} = \frac{u_{LBM} L_{LBM}}{\upsilon_{LBM}} \tag{12}$$

where Re is the Reynolds number, L is the characteristic length.

Before the beginning of the simulation, there is no velocity distribution in the fracture. In the simulation, the CO_2 flow will reach a steady state after some time and the velocities at steady state will be used for further calculation and analysis. For example, Fig. 9 shows the velocity vector distributions for the time t_a = 40, 000 and 50, 000ts being the same in Lattice Boltzmann domain, which means the flow has reached the steady state. It can be seen that Figs. 8 and 9 strictly follow the fracture aperture distributions in Fig. 2. In Fig. 8, there is an area of fracture aperture that is pretty narrow on the injecting surface, which corresponds to fracture aperture distribution of the deepest blue color on the injecting surface in Fig. 2. In addition, there is a large blank area on velocity distributions in Fig. 9, which is located at about 14–20 mm in X direction and 16–22 mm in Y direction. In Fig. 2, this area on the X-Y plane has deep blue colors that means the apertures are very small and the flow prefers other flow paths with larger apertures. Three points a, b and c locating at 20.15625, 20.625 and 21.09375 mm at Y direction are used to generate the corresponding aperture and velocity distributions along X direction, which is shown in Fig. 10. The Location a, b and c all belongs to the range of the blank area mentioned above. In Fig. 10, it can be seen that the apertures from 14 to 16 mm along X direction are much smaller and the velocities equal to zero, which reflects the existence of the blank area in Fig. 9.

5. Results analysis

In Fig. 10, it is shown that the average velocity and tortuosity correspond to different pressure conditions at the temperature of 20, 60 and 100 °C with the pressure difference between the injecting and discharging surfaces (Δp) being 10 Pa. The tortuosity can be calculated based on the following equation [75,76]:

$$Tortuosity = \frac{\sum |V(x, y, z)|}{\sum |V_x(x, y, z)|} \tag{13}$$

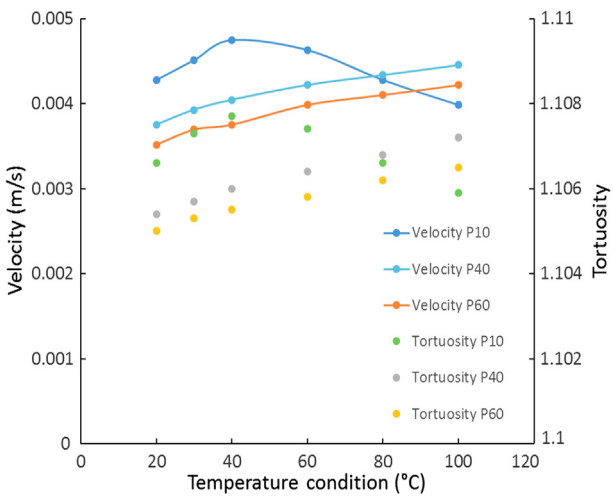

Fig. 14. Velocity and tortuosity for different temperature conditions with $\Delta p = 10$ Pa.

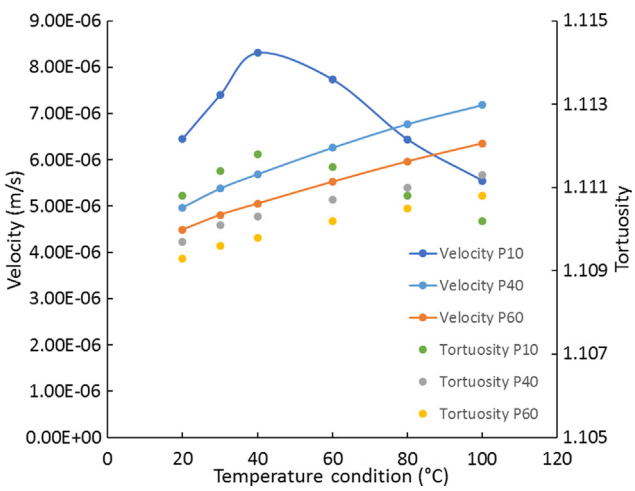

Fig. 15. Velocity and tortuosity for different temperature conditions with $\Delta p = 0.01$ Pa.

where $|V_x(x, y, z)|$ is the magnitude of velocity in X direction that is the main flow direction and $|V(x, y, z)|$ is the magnitude of velocity vector at a certain location with the coordinates of (x, y, z):

$$|V(x, y, z)| = \sqrt{V_x(x, y, z)^2 + V_y(x, y, z)^2 + V_z(x, y, z)^2} \tag{14}$$

The values of velocity can be gained directly from LBM simulations and then transformed into the real physical units. It can be seen that, with corresponding to the kinematic viscosities, the average velocity for the temperature conditions T = 20 and 60 °C both have gradually decreasing trends with the increase of pressure conditions and the average velocity for T = 100 °C increases initially and then decreases in Fig. 11. The kinematic viscosity refers to the ratio of dynamic viscosity to density. For three temperature conditions, the values of the average velocity are around 0.004 and 0.005 m/s. In addition, the average velocity values of T = 60 °C are always larger than those of T = 20 °C. However, the values for T = 100 °C show a sudden hump with the changes of temperatures. The tortuosity has the same trend to the average velocity for each temperature condition. The values of tortuosity locate in the range of 1.104–1.108. Fig. 12 shows the average velocity and tortuosity under the same pressure and temperature conditions with $\Delta p = 0.01$ Pa. With the same changing trends, the values of the average velocity are much smaller and the values of tortuosity for three temperature conditions become a little larger compared with the results in Fig. 11. Figs. 11 and 12 show that the average velocity and tortuosity of liquid and supercritical CO_2 for different pressure conditions change with changing temperature.

Fig. 13 is an example of streamlines for two pressure conditions P = 10 and 60 MPa with the temperature condition T = 20 and 100 °C. Under these conditions, the CO_2 are at liquid and supercritical state respectively. As it is known, tortuosity is the ratio of the length of a streamline—a flow line or path—between two points to the straight-line distance between those points. It should be noticed that velocity distributions in Fig. 9 and streamlines in Fig. 13 both reflect the preferential flow paths of liquid and supercritical CO_2 flow through fracture rough surfaces, which also represent CO_2 concentration on fracture rough surfaces because it can be seen that there is no liquid and supercritical CO_2 flow on some areas on the fracture rough surface based on simulation results. In Fig. 13, small differences of streamlines that reflect the tortuosity between two cases are caused by the changes of pressure conditions. And it can be found that the time for streamlines shaping varies when the pressure condition equals to 10 and 60 MPa from time legends next to the streamline distributions. The area that is surrounded by red borders showing that the streamlines for P = 60 MPa in this area become more tortuous than those for P = 10 MPa when the temperature equals to 20. As for T = 100 °C, the comparison of streamlines do not show obvious differences. In addition to direct observations from the streamlines distributions, the tortuosity values of the area surrounded by red borders are calculated and compared with the tortuosity values of the whole fracture. As for the tortuosity calculations in the surrounded area, the grids from 60 to 90 along Y direction and from 175 to 225 along X direction are chosen. In this area, the values of tortuosity for the temperature 20 and 100 °C under the pressure condition 10 MPa are 1.1754 and 1.1742 respectively and those under the pressure condition 60 MPa are 1.1785 and 1.1755. And the differences of the tortuosity values for the whole area of the fracture surfaces between 10 MPa and 60 MPa for the temperature 20 and 100 °C are 0.0016 and 0.0006. Table 1 shows a direct compassion for better understanding. So it is obvious that the differences of the tortuosity values between 10 MPa and 60 MPa in the surrounded area are much larger than those in the whole fracture, which are reflected on the observed streamlines distributions. Based on the above analysis, the tortuosity has a tight relationship with the pressure conditions with considering the average velocities being similar.

For Figs. 14 and 15, the temperature range is from 20 °C to 100 °C and corresponding pressures are set as 10, 40 and 60 MPa. The relationships between the average velocity and temperature in both Figs. 14 and 15 show increasing trends with the increase of temperature for P = 40 and 60 MPa, which is because the kinematic viscosities of liquid and supercritical CO_2 in this temperature range decreases while the temperature becomes larger. The values of the average velocity equals to about 0.004 m/s with $\Delta p = 10$ Pa and P = 40 MPa and the values for P = 60 MPa is a little smaller than those of P = 40 MPa. Similarly, when $\Delta p = 0.01$ Pa, the velocity values of P = 40 MPa are larger than those of P = 60 MPa. And the average velocity for P = 10 MPa shows an irregular trend, increasing and then decreasing with the increase of temperature. As for tortuosity, the curves have almost same trends to the average velocity curves. In addition, the tortuosity with $\Delta p = 0.01$ Pa is larger compared with tortuosity with $\Delta p = 10$ Pa. Figs. 14 and 15 summarize the liquid and supercritical CO_2 flow for the temperature between 20 °C and 100 °C in responses to $\Delta p = 10$ and 0.01 Pa respectively under the pressure condition 10, 40 and 60 MPa. It can be concluded that the tortuosity is also tightly related to the temperature.

Fig. 16 gives an illustration of streamlines for T = 20 and 100 °C with $\Delta p = 0.01$ Pa for two pressure conditions. It can be seen that the time that streamlines flow through rough fracture surfaces are different, which also reflect the effects of different temperatures. When temperature equals to 20 °C, the CO_2 stays at liquid state and supercritical CO_2 appears with the temperature being 100 °C. As is stated above, the increase of temperature leads to the increase of tortuosity. The

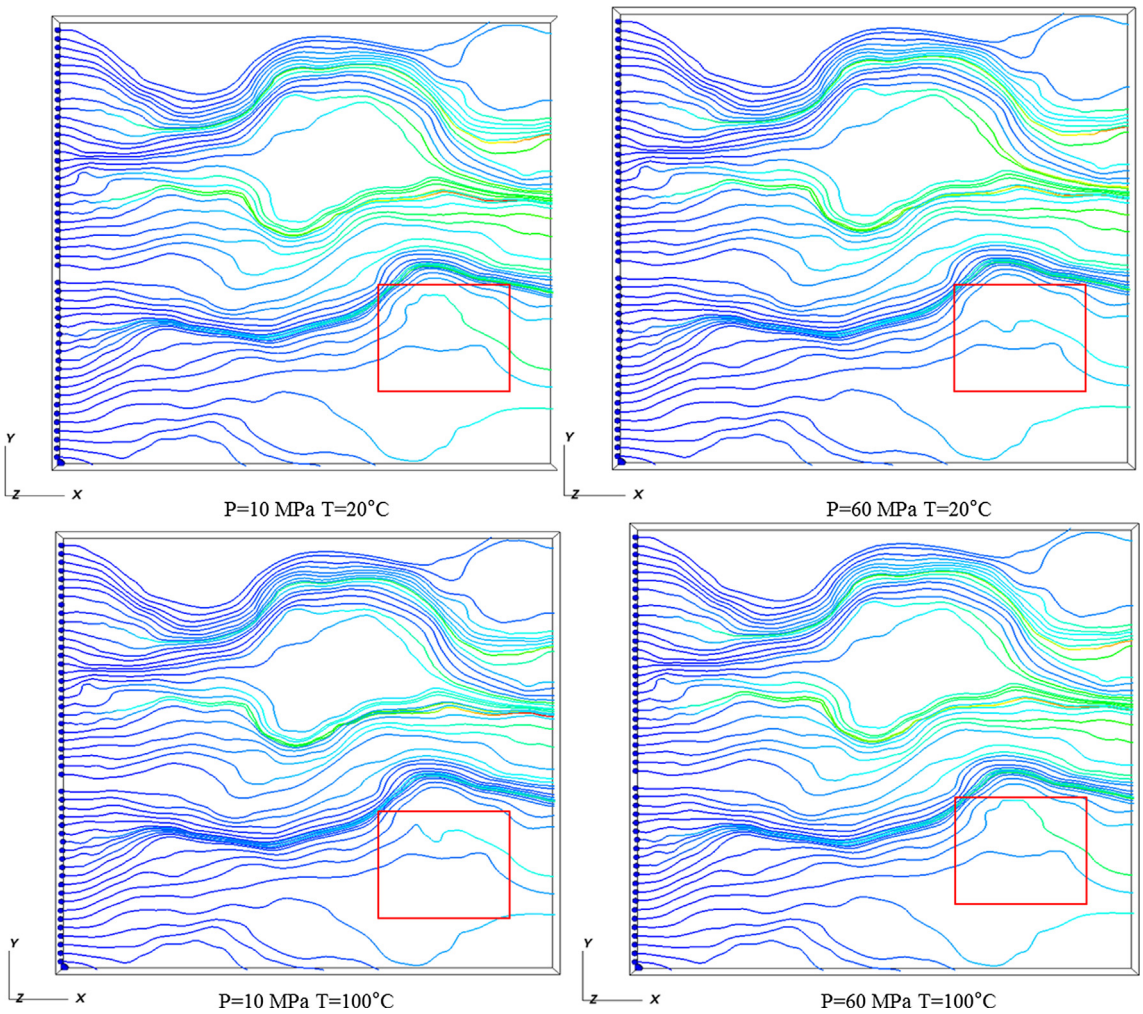

Fig. 16. Streamlines for T = 20 and 100 °C with P = 10 and 60 MPa and Δp = 0.01 Pa.

Table 2
Comparisons of tortuosity differences between the surrounded and whole areas at different temperature conditions.

	Tortuosity of T = 20 °C	Tortuosity of T = 100 °C	Tortuosity differences in the surrounded area	Tortuosity differences of the whole area
P = 10 MPa	1.1899	1.1928	0.0029	0.0006
P = 60 MPa	1.1832	1.1791	0.0041	0.0013

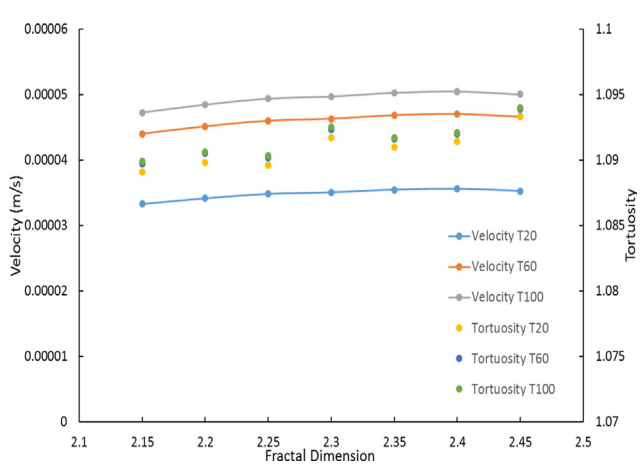

Fig. 17. Velocity and tortuosity for different fractal dimensions with the pressure condition 20 MPa.

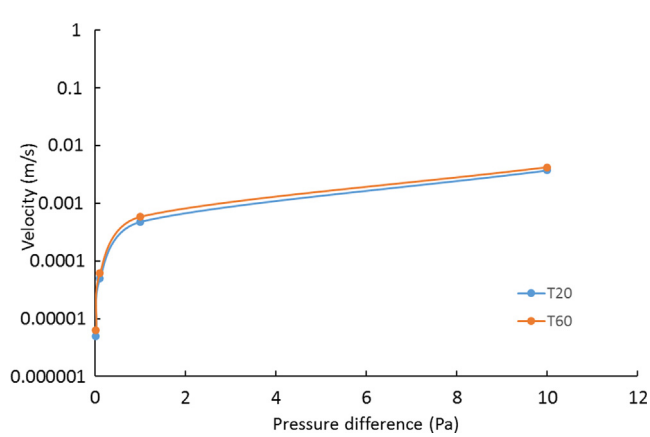

Fig. 18. Semi-log relationships between velocity and Δp for different temperature conditions with P = 40 MPa.

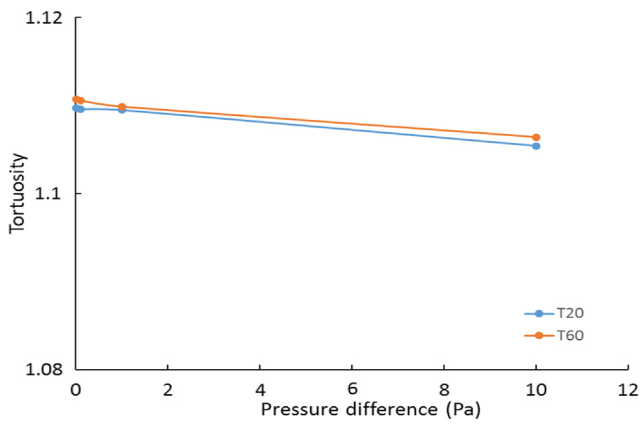

Fig. 19. The relationship between tortuosity and Δp for different temperature conditions with P = 40 MPa.

increases of tortuosity reflected in Fig. 16 shows that the small proportion of streamlines become more tortuous for P = 60 MPa. When pressure equals to 60 MPa, the tortuosity has a positive relationship with the temperature. With the pressure condition being 10 MPa, the streamlines for T = 20 °C are a little more tortuous than the streamlines for T = 100 °C because the kinematic viscosity for T = 20 °C is smaller than that for T = 100 °C. From the perspective of quantifying the tortuous behavior, the differences of the tortuosity values for the pressure condition 10 and 60 MPa equal to 0.0006 and 0.0013 respectively. However, the corresponding differences of tortuosity values are much larger: 0.0029 and 0.0041 (The tortuosity values of the temperature 20 °C equal to 1.1899 and 1.1832 and the tortuosity values of the temperature 100 °C are 1.1928 and 1.1791), as is shown in Table 2.

In addition, it can be found that the average velocity and tortuosity curves for the pressure condition P = 40 MPa are both located higher than those for P = 60 MPa in Figs. 14 and 15. Similarly, the average velocity and tortuosity curves for the temperature T = 60 °C are higher than those for T = 20 °C. To summarize, the results shown in Figs. 14 and 15 and the results from Figs. 11 and 12 provide mutual validations.

In addition to the grid resolution validation, the validations of fracture surface roughness (geometry) and scales of the fracture model size are also needed for consideration. A fracture model with its size being 6.4 × 6.4 mm is used here. Similarly, the X-Y plane is divided into 128 × 128 grids. Fig. 17 shows the average velocity and tortuosity curves changes with the increase of the fractal dimension that is used to generate corresponding fracture surface roughness for different temperatures (20, 60 and 100 °C) under the same pressure condition P = 20 MPa. The values of the fractal dimension are from 2.15 to 2.45 with the interval being 0.05. It can be found that the differences among the values of the average velocity and tortuosity for different temperatures are almost same with corresponding to different fractal dimensions, which validate results shown in above figures. Furthermore, the velocity and tortuosity correlations don't show similar trends with the increasing fractal dimensions, which is different from Figs. 11, 12, 14 and 15. This reflects that the average velocity and tortuosity curves have similar trends due to the CO_2 density determined by the pressure and temperature conditions, not affected by the fracture surface

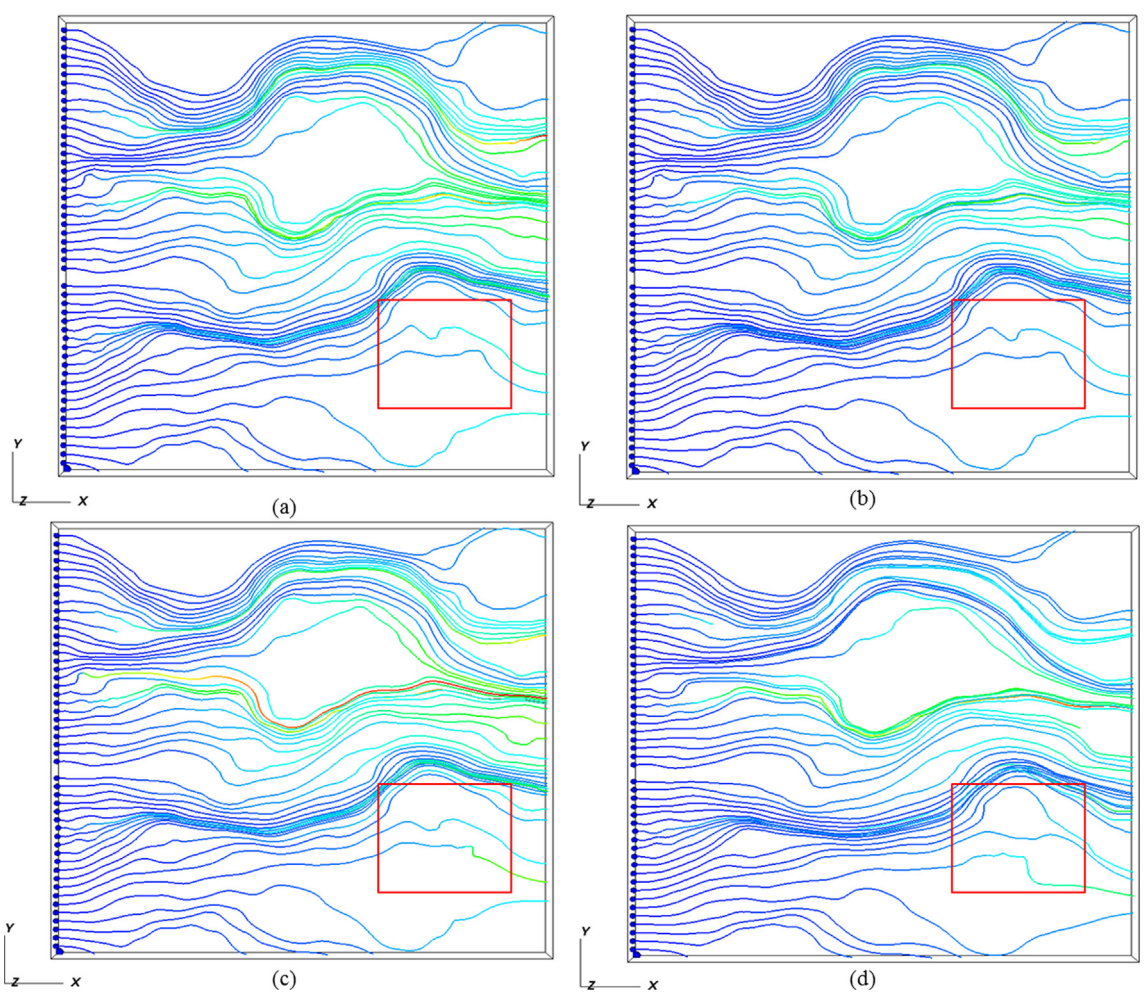

Fig. 20. Streamlines for different Δp(a: 0.01 Pa; b: 0.1 Pa; c: 1 Pa; d: 10 Pa) with P = 40 MPa and T = 20 °C.

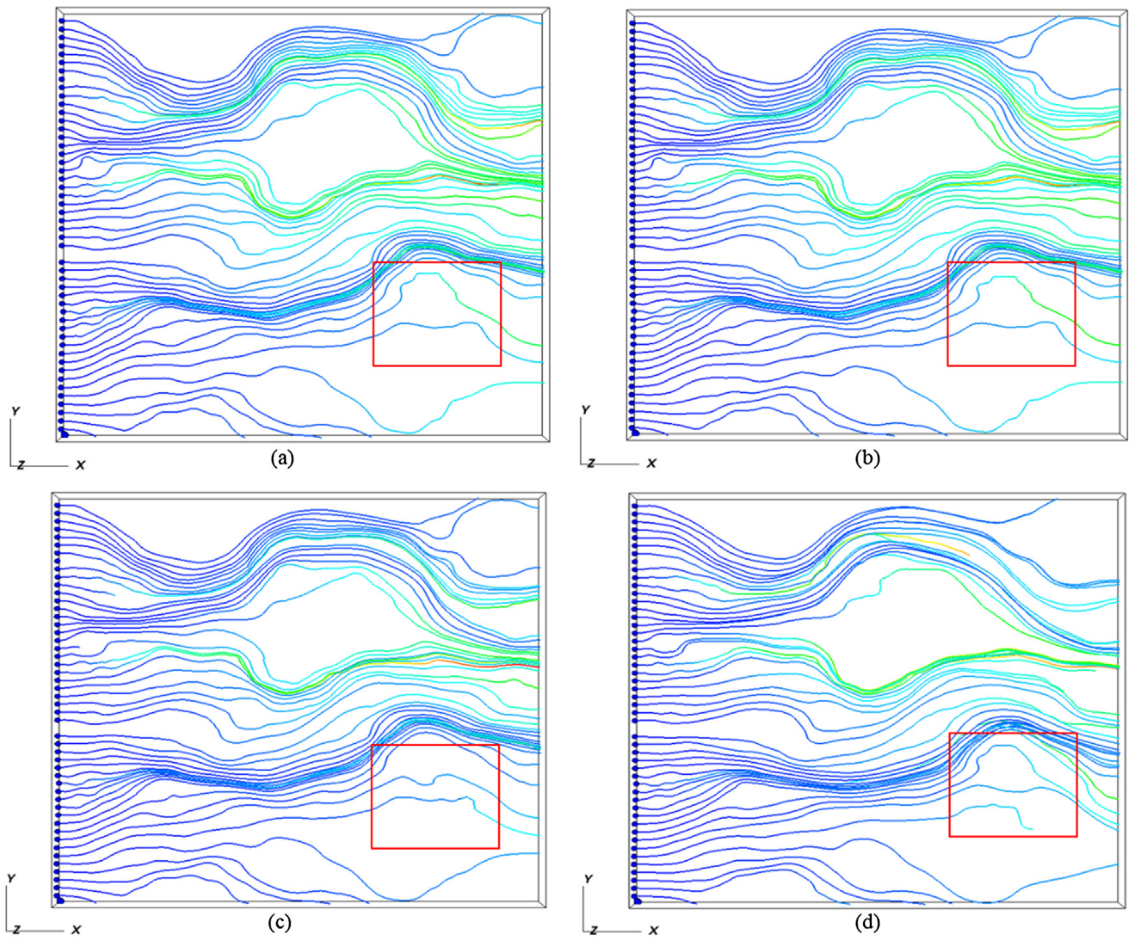

Fig. 21. Streamlines for different Δp (a: 0.01 Pa; b: 0.1 Pa; c: 1 Pa; d: 10 Pa) with P = 40 MPa and T = 60 °C.

roughness (geometry).

In Fig. 18, two semi-log curves for different values of the pressure difference Δp with the temperature T = 20 and 60 °C under the condition of P = 40 MPa is shown. The values of Δp include: 10, 1, 0.1 and 0.01 Pa. The semi-log curves are adopted in order to have a better identification for the differences of velocities amongΔp values. The average velocity values for T = 60 °C are larger than those for T = 20 °C because the kinematic viscosity for T = 60 °C is smaller than that for T = 20 °C. And the average velocity values increase with the pressure difference becoming larger. Fig. 19 shows that the tortuosity become smaller with the increase of the pressure difference. And the values of tortuosity varies around 1.115. And the tortuosity for T = 60 °C is larger than the tortuosity for T = 20 °C. This is because the kinematic viscosity for T = 60 °C is smaller than that for T = 20 °C when the pressure equals to 40 MPa.

Figs. 20 and 21 show the differences of streamlines corresponding to four pressure differences for the temperature T = 20 and 60 °C respectively, playing a complementary role in demonstrating the changes of tortuosity in Figs. 18 and 19. In both Figs. 20 and 21, there are differences in streamlines that can be observed to certain extent. The streamlines surrounded by red borders are almost the same in both Figs. 20 and 21, which are reflected in the calculation results of tortuosity differences. The tortuosity differences of the whole fracture between the pressure difference 0.01 and 10 Pa for the temperature 20 and 60 °C both equal to 0.0043, which are similar to the tortuosity differences of the surrounded area (0.0057 and 0.0063). In addition, the streamlines in the area surrounded by the red border are easy to be seen the extent of concentrations from 0.01 to 10 Pa. At these cases, with the temperature and pressure conditions remaining constant, various velocities that are determined by Δp result in different streamlines. When the average velocity increases by scales in these cases, the streamlines become more concentrated. As a result, the tortuosity decreases with the upscale of the average velocity.

Figs. 18–21 give detailed illustrations that the tortuosity becomes smaller and streamlines become more concentrated due to the upscaling velocity that is caused by different sets of the pressure difference with combination of the streamline distributions, which is also validated by the above results.

6. Conclusions

It is the first time to investigate the effects of liquid and supercritical CO_2 properties on flow behaviors through a single 3D self-affine rough fracture by using the Lattice Boltzmann method. A D3Q19 LBM code has been programmed to generate the numerical fracture model that gives an accurate reflection of fracture surface roughness and to simulate the liquid and supercritical CO_2 flow under various pressure and temperature conditions with certain pressure differences between injecting and discharging surfaces. The different properties of liquid and supercritical CO_2 were calculated by Peng-Robinson Equation of State through changing relevant pressures and temperatures. Different CO_2 properties were used to generate corresponding average velocity and tortuosity curves and was used to generate the velocity and streamlines distributions under various pressure differences. The streamlines distributions show an irregular pattern due to the rough fracture surfaces and play a significant role in analysing relevant tortuosity changes. It was found that the average velocity and tortuosity have tight relationships with temperature and pressure conditions while other

conditions keep constant, which were validated mutually. The streamlines tend to be more tortuous with the gradual increase of the kinematic viscosity when average velocities are similar at the same scale. The tortuosity decreases with the upscaling of average velocity. With upscaling the average velocity, the streamlines become more concentrated for the same CO_2 properties. In addition, it has been proven that the similar trends of the average velocity and tortuosity curves are not affected by the fracture surface roughness. This paper provides an efficient and accurate evaluation of the effects of CO_2 properties on flow behaviors at low velocities through a rough fracture, which has a great significance in the natural and induced fracture reservoirs for the purposes of CO_2 storage, enhanced shale gas/oil recovery and enhanced geothermal systems.

References

[1] Grimston MC, Karakoussis V, Fouquet R, van der Vorst R, Pearson P, Leach M. The European and global potential of carbon dioxide sequestration in tackling climate change. Climate Policy 2001;1(2):155–71.

[2] Li ZW, Dong MZ, Li SL, Huang S. CO_2 sequestration in depleted oil and gas reservoirs—caprock characterization and storage capacity. Energy Convers Manage 2006;47(11–12):1372–82.

[3] Global CCS Institute. Introduction to industrial carbon capture and storage. Global Status of CCS 2016: Special Report.

[4] Milan JP, Eric FM, Michael LJ. High-fidelity reservoir simulations of enhanced gas recovery with supercritical CO_2. Energy 2016;111:548–59.

[5] Sun XH, Wang ZY, Sun BJ, Wang WD. Research on hydrate formation rules in the formations for liquid CO_2 fracturing. J Nat Gas Sci Eng 2016;33:1390–401.

[6] Brown DW. A hot dry rock geothermal energy concept utilizing supercritical CO2 instead of water. In: Proceedings of the Twenty-Fifth Workshop on Geothermal Reservoir Engineering, Stanford University, CA, January 24–26, 2000, SGP-TR-165.

[7] Fouillac C, Sanjuan B, Gentier S, Czernichowski-Lauriol I. Could sequestration of CO2 be combined with the development of Enhanced Geothermal Systems? In: Third Annual Conference on Carbon Capture and Sequestration, Alexandria, VA, May 3–6, 2004.

[8] Pruess K. Enhanced geothermal systems (EGS) using CO_2 as working fluid – a novel approach for generating renewable energy with simultaneous sequestration of carbon. Geothermics 2006;35:351–67.

[9] Wang F, Fu SF, Guo G, Jia ZZ, Luo SJ, Guo RB. Experimental study on hydrate-based CO_2 removal from CH_4/CO_2 mixture. Energy 2016;104:76–84.

[10] Liu YG, Hou J, Zhao HF, Liu XY, Xia ZZ. A method to recover natural gas hydrates with geothermal energy conveyed by CO_2. Energy 2018;144:265–78.

[11] Alvarado V, Manrique E. Enhanced oil recovery: an update review. Energies 2010;3:1529–75.

[12] Shukla R, Ranjith P, Haque A, Choi X. A review of studies on CO_2 sequestration and caprock integrity. Fuel 2010;89(10):2651–64.

[13] Xu RN, Zhang L, Zhang FZ, Jiang PX. A Review on heat transfer and energy conversion in the enhanced geothermal systems with water/CO2 as working fluid. Int J Energy Res 2015;39(13):1722–41.

[14] Tudor R, Vozniak C, Peters W, Banks ML. Technical advances in liquid CO2 fracturing. In: Annual Technical Meeting, June 12–15, 1994, Calgary, Alberta. PETSOC-94-36.

[15] Michael GT, Richard EM. A comparison of results of three different CO2 energized frac fluids: a case history. In: SPE Gas Technology Symposium, April 30-May 2, 2002, Calgary, Alberta, Canada. SPE-75681-MS.

[16] Lu M, Connell LD. The transient behavior of CO_2 flow with phase transition in injection wells during geological storage – application to a case study. J Petroleum Sci Eng 2014;124:7–18.

[17] Zhang XW, Lu YY, Tang JR, Zhou Z, Liao Y. Experimental study on fracture initiation and propagation in shale using supercritical carbon dioxide fracturing. Fuel 2017;190:370–8.

[18] Ishida T, Chen YQ, Bennour Z, Yamashita H, Inui S, Nagaya Y, Naoi M, Chen Q, Nakayama Y, Nagano Y. Features of CO2 fracturing deduced from acoustic emission and microscopy in laboratory experiments. J Geophys Res: Solid Earth 2016;121(11):8080–98.

[19] Zhang L, Jiang PX, Wang ZC, Xu RN. Convective heat transfer of supercritical CO2 in a rock fracture for enhanced geothermal systems. Appl Therm Eng 2017;115:923–36.

[20] Meier P, Ivory J, Rocco M, Scott K. Field and laboratory measurements of leakoff parameters for liquid CO2 and liquid CO/N fracturing. In: Annual Technical Meeting, June 8–11, 1997, Calgary, Alberta. PETSOC-97-105.

[21] Zou YS, Li N, Ma XF, Zhang SC, Li SH. Experimental study on the growth behavior of supercritical CO_2-induced fractures in a layered tight sandstone formation. J Nat Gas Sci Eng 2018;49:145–56.

[22] Zhou X, Burbey TJ. Fluid effect on hydraulic fracture propagation behavior: a comparison between water and supercritical CO_2-like fluid. Geofluids 2014;14(2):174–88.

[23] Borgia A, Oldenburg CM, Zhang R, Pan LH, Daley TM, Finsterle S, et al. Simulations of CO_2 injection into fractures and faults for improving their geophysical characterization at EGS sites. Geothermics 2017;69:189–201.

[24] Wang JT, Sun BJ, Li H, Wang X, Wang ZY, Sun XH. Phase state control model of supercritical CO_2 fracturing by temperature control. Int J Heat Mass Transf 2018;118:1012–21.

[25] Lomize GM. Flow in fractured rocks (in Russian). Moscow, Russia: Gesemergoizdat; 1951.

[26] Gangi AF. Variation of whole and fractured porous rock permeability with confining pressure. Int J Rock Mech Mining Sci Geomech Abstracts 1978;15(5):249–57.

[27] Berkowitz B, Braester C. Solute transport in fracture channel and parallel plate models. Geophys Res Lett 1991;18(2):227–30.

[28] Liu ZY, Chen M, Zhang GQ. Analysis of the influence of a natural fracture network on hydraulic fracture propagation in carbonate formations. Rock Mech Rock Eng 2014;47(2):575–87.

[29] Lanaro F. A random field model for surface roughness and aperture of rock fractures. Int J Rock Mech Min Sci 2000;37(8):1195–210.

[30] Gouze P, Noiriel C, Bruderer C, Loggia D, Leprovost R. X-ray tomography characterization of fracture surfaces during dissolution. Geophys Res Lett 2003;30(5):1267.

[31] Muralidharan V, Chakravarthy D, Putra E, Schechter DS. Investigating fracture aperture distributions under various stress conditions using X-Ray CT scanner. In: Canadian International Petroleum Conference, June 8–10, 2004, Calgary, Alberta, Canada. PETSOC-2004-230.

[32] Qian J, Zhan H, Zhao W, Sun F. Experimental study of turbulent unconfined groundwater flow in a single fracture. J Hydrol 2005;311(1–4):134–42.

[33] Qian J, Chen Z, Zhan H, Guan H. Experimental study of the effect of roughness and Reynolds number on fluid flow in rough-walled single fractures: a check of local cubic law. Hydrol Process 2011;25(4):614–22.

[34] Su GW, Geller JT, Pruess K, Wen F. Experimental studies of water seepage and intermittent flow in unsaturated, rough-walled fractures. Water Resour Res 1999;35(4):1019–37.

[35] Noiriel C, Gouze P, Made B. 3D analysis of geometry and flow changes in a limestone fracture during dissolution. J Hydrol 2013;486:211–23.

[36] Tsang CF, Neretnieks I. Flow channeling in heterogeneous fractured rocks. Rev Geophys 1998;36(2):275–98.

[37] Co CKD, Pollard DD, Horne RN. Towards a better understanding of the impact of fracture roughness on permeability-stress relationships using first principles. 2017 42nd Stanford Geothermal Workshop Proceedings.

[38] Hakami E, Larsson E. Aperture measurements and flow experiments on a single natural fracture. Int J Rock Mech Mining Sci 1996;33(4):395–404.

[39] Abelin H, Birgersson L, Widen H, Aagren T, Moreno L, Neretnieks I. Channelling experiment. Technical report. Swedish Nuclear Fuel and Waste Management Company; 1990.

[40] Watanabe N, Hirano N, Tsuchiya N. Determination of aperture structure and fluid flow in a rock fracture by high-resolution numerical modelling on the basis of a flow-through experiment under confining pressure. Water Resour Res 2008;44(6):W06412.

[41] Brown SR. Fluid flow through rock joints the effect of surface roughness. J Geophys Res 1987;92(B2):1337–47.

[42] Zimmerman RW, Kumar S, Bodvarsson GS. Lubrication theory analysis of the permeability of rough-walled fractures. Int J Rock Mech Mining Sci Geomech Abstracts 1991;28(4):325–31.

[43] Brush DJ, Thomson NR. Fluid flow in synthetic rough-walled fractures: Navier-Stokes, Stokes, and local cubic law simulations. Water Resour Res 2003;39(4):1085.

[44] Yeo IW, Ge S. Applicable range of the Reynolds equation for fluid flow in a rock Fracture. Geosci J 2005;9(4):347–52.

[45] Ishibashi T, Watanabe N, Hirano N, Okamoto A, Tsuchiya N. Upgrading of aperture model based on surface geometry of natural fracture for evaluating channeling flow. GRC Trans 2012;36:481–6.

[46] Wang L, Cardenas MB, Slottke DT, Ketcham RA, Sharp JM. Modification of the Local Cubic Law of fracture flow for weak inertia, tortuosity, and roughness. Water Resour Res 2015;51(4):2064–80.

[47] Kim J, Gao X, Srivatsan TS. Modeling of crack growth in ductile solids: a three-dimensional analysis. Int J Solids Struct 2003;40:7357–74.

[48] Tan YF, Zhou ZF. Simulation of solute transport in a parallel single fracture with LBM/MMP mixed method. J Hydrodyn 2008;20(3):365–72.

[49] Eker E, Akin S. Lattice Boltzmann simulation of fluid flow in synthetic fractures. Transp Porous Media 2006;65(3):363–84.

[50] Dou Z, Zhou Z, Sleep BE. Influence of wettability on interfacial area during immiscible liquid invasion into a 3D self-affine rough fracture: lattice Boltzmann simulations. Adv Water Resour 2013;61:1–11.

[51] Wang M, Chen Y, Ma G, Zhou J, Zhou C. Influence of surface roughness on nonlinear flow behaviors in 3D self-affine rough fractures: lattice Boltzmann simulations. Adv Water Resour 2016;96:373–88.

[52] Briggs S, Karney BW, Sleep BE. Numerical modeling of the effects of roughness on flow and eddy formation in fractures. J Rock Mech Geotech Eng 2017;9:105–15.

[53] Li JW, Claudi C, Sergio GT, Li Z, Li L. Laboratory investigation of flow paths in 3D self-affine fractures with Lattice Boltzmann simulations. Energies 2018;11(1):168.

[54] Neuville A, Toussaint R, Schmittbuhl J. Fracture roughness and thermal exchange: a case study at Soultz-sous-Forêts. CR Geosci 2010;342(78):616–25.

[55] He Y, Bai B, Hu S, Li X. Effects of surface roughness on the heat transfer characteristics of water flow through a single granite fracture. Comput Geotech

2016;80:312–21.
[56] Luo S, Zhao Z, Peng H, Pu H. The role of fracture surface roughness in macroscopic fluid flow and heat transfer in fractured rocks. Int J Rock Mech Min Sci 2016;87:29–38.
[57] Fox DB, Koch DL, Tester JW. The effect of spatial aperture variations on the thermal performance of discretely fractured geothermal reservoirs. Geothermal Energy 2015;3:21.
[58] Huang SL, Oelfke SM, Speke RC. Applicability of fractal characterization and modelling to rock joint profiles. Int J Rock Mech Mining Sci Geomech Abstracts 1992;29(2):89–98.
[59] Odling NE. Natural fracture profiles, fractal dimension and joint roughness coefficients. Rock Mech Rock Eng 1994;27(3):135–53.
[60] Schmittbuhl J, Steyer A, Jouniaux L, Toussaint R. Fracture morphology and viscous transport. Int J Rock Mech Min Sci 2008;45(3):422–30.
[61] Mandelbrot BB. The fractal geometry of nature. San Francisco: Freeman; 1982.
[62] Mandelbrot BB. Self-affine fractals and fractal dimension. Phys Scripta 1985;32:257–60.
[63] Molz F, Liu H, Szulga J. Fractional Brownian motion and fractional Gaussian noise in subsurface hydrology: a review, presentation of fundamental properties, and extensions. Water Resour Res 1997;33(10):2273–86.
[64] Babadagli T, Ren X, Develi K. Effects of fractal surface roughness and lithology on single and multiphase flow in a single fracture: an experimental investigation. Int J Multiph Flow 2015;68:40–58.
[65] Power WL, Tullis TE, Brown SR, Boitnott GN, Scholz CH. Roughness of natural fault surfaces. Geophys Res Lett 1987;14(1):29–32.
[66] Ogilvie SR, Isakov E, Glover PWJ. Fluid flow through rough fractures in rocks. II: A new matching model for rough rock fractures. Earth Planet Sci Lett 2006;241(3–4):454–65.
[67] Succi S. The Lattice Boltzmann Equation for fluid dynamics and beyond. Clarendon Press, Oxford University; 2001.
[68] Qian YH, d'Humieres D, Lallemand P. Lattice BGK models for Navier-Stokes equation. Europhys Lett 1992;17(6):479.
[69] Okabe H, Blunt MJ. Prediction of permeability for porous media reconstructed using multiple-point statistics. Phys Rev E 2004;70:066135.
[70] Shi XY, Gao H, Lazouskaya VI, Kang Q, Jin Y, Wang LP. Viscous flow and colloid transport near air-water interface in a microchannel. Comput Math Appl 2010;59:2290–304.
[71] Li Q, Luo KH, Kang QJ, He YL, Chen Q, Liu Q. Lattice Boltzmann methods for multiphase flow and phase-change heat transfer. Prog Energy Combust Sci 2016;52:62–105.
[72] He X, Luo LS. Lattice Boltzmann model for the incompressible Navier-Stokes equation. J Stat Phys 1997;88(3–4):927–44.
[73] Mohamad AA. Lattice Boltzmann method: fundamentals and engineering applications with computer codes. London: Springer-Verlag; 2011.
[74] Huang H, Sukop M, Lu X. Multiphase lattice Boltzmann methods: theory and application. John Wiley & Sons; 2015.
[75] Duda A, Koza Z, Matyka M. Hydraulic tortuosity in arbitrary porous media flow. Phys Rev E 2011;84:036319.
[76] Sheikh B, Pak A. Numerical investigation of the effects of porosity and tortuosity on soil permeability using coupled three-dimensional discrete-element method and lattice Boltzmann method. Phys Rev E 2015;91:053301.